Proofing your Book Chapter

The following contains the PDF proof of your book chapter for you to review. Please follow the steps below to proof your chapter.

1. Read through your chapters carefully

- Remember to check that:
  - **special characters** appear correctly, especially in equations
  - **Figures and Tables** are correct
  - **headings and sub-headings** are placed correctly
- Our staff will not read through your chapters in detail once you have returned it, so please make sure you have checked everything. Final responsibility for content lies with the author.
- As no revised proofs will be provided, please ensure all required corrections are indicated at this stage.

2. Mark up any corrections that are required

- Please only correct scientific or grammatical errors in your chapters – **do not** rewrite sections or make minor cosmetic changes at this stage.
- Please use the **annotation tools** to mark up corrections on the PDF proof – further instructions can be found on the following page.
- Please do not edit the PDF directly or send a list of corrections.
- If any replacement figures are required, please resupply the file at the highest possible resolution.
- Please **only supply new versions of figures if you have been requested to do so, or you need to supply a corrected version.**
- Permission statements for reproduced material may have been edited to meet the different requirements of the copyright holders. Please do not correct the formatting of these statements.

3. Make sure you have answered all author queries

- These are listed before the beginning of each chapter– click on the query number to jump to the relevant place in the text.
- **Please put your responses in the text, not on the query page.**

4. Return your corrected proof to us

- Please email the annotated PDF of your chapter to booksprod@rsc.org within ONE WEEK of receipt.
- Please do not return your proof to the email address from which you received the download link, or to your editor.

If you have any queries, please do not hesitate to contact us at booksprod@rsc.org

How to Annotate your PDF Proof

Note: The location and appearance of tools may vary depending on the software you are using to read your proof. We recommend using Adobe Acrobat Reader DC (as shown in the screenshots below), which can be downloaded for free online.

The **Comment** function can be found in the **right-hand sidebar**, which should appear when you open your PDF.
Otherwise, in the View menu, click '**Tools**' and then select '**Comment**'. This will make the **Comment tools** visible (shown below).

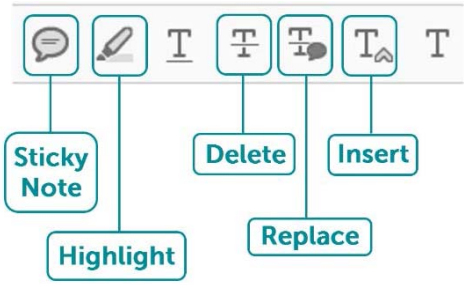

Select the piece of text that you want to mark up, and then click on the relevant Tool button to add the mark up to the text.

For the Insert, Replace, and Sticky Note tools, this will open up a Note in **which you can add instructions, or the text to be replaced/inserted –** otherwise, you can double-click on the mark-up to open this.

For all tools, any instructions you've added will appear in the Comment sidebar – you can also double-click on this to change, add to or remove the instructions.

Replace

Use the Replace tool to indicate text that should be changed.

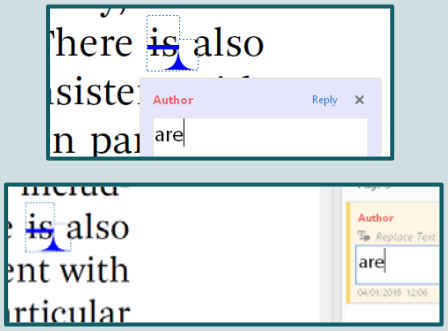

Insert

Use the Insert tool to provide new text.

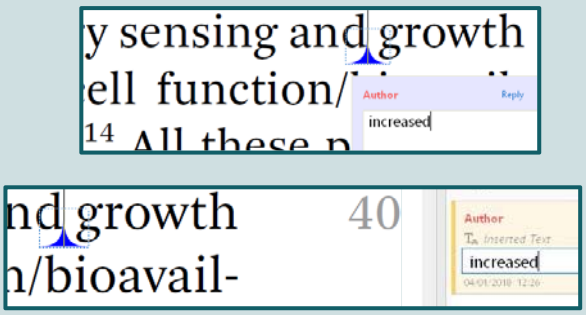

Delete

Use the Delete tool to indicate text that needs to be removed completely.

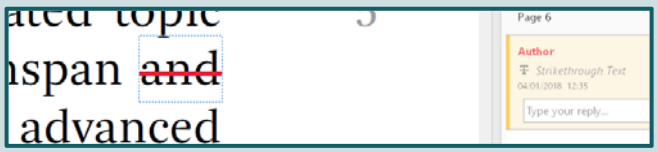

Highlight

Use the Highlight tool to indicate formatting changes to text.

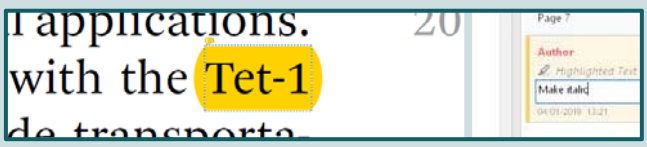

Sticky Note

Use the Sticky Note tool to respond to a query, or indicate a change that cannot be marked up using one of the tools above.

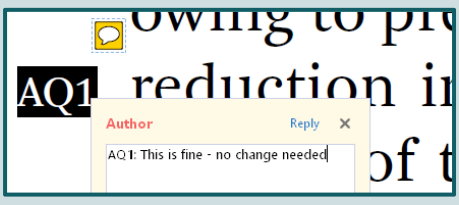

Hints and tips

Special characters can be pasted into corrections from the Character Map in your operating system.

Text can be made **bold** and **italic** using shortcut keys Ctrl+B and Ctrl+I.

If you have difficulty selecting all the text you wish to correct, try holding down the Shift key and using the arrow keys.

AUTHOR QUERY FORM

Book Title: Photochemistry: Volume 52
Chapter Title: Mechanistic investigation of light-driven catalysis for solar fuel formation

Please indicate the changes required in response to the queries within the text. If no changes are needed please clearly state this next to the query marker.

AQ1 Ref. 30: Can this reference be updated?

Mechanistic investigation of light-driven catalysis for solar fuel formation

Mirco Natali*[a] and Andrea Sartorel*[b]

DOI: 10.1039/9781837676552-00374

Solar energy conversion into chemical fuels currently represents a viable solution to the global energy issue. In this regard, water splitting with formation of dihydrogen as an energy carrier has been usually considered as a target reaction. Due to the mechanistic complexity associated with both the oxidation (oxygen evolving reaction, OER) and reduction (hydrogen evolving reaction, HER) half-reactions, the design of active catalysts and their efficient coupling with photoactive components appears as a major target. Optical spectroscopies turn out to be key tools to monitor the photoreaction dynamics and extract detailed kinetic data which can be profitably employed towards performance optimization of both catalytic routines. This chapter will describe the application of steady-state and time-resolved absorption and emission spectroscopy to the investigation of the mechanistic aspects associated with both the OER and HER performed using molecular components both as light-harvesting and catalytic units. Through the case studies examined, we will give an overview of how these spectroscopic tools allow proper identification of the photoreaction mechanism, the rate and efficiency of each (photo)chemical step, the possible involvement of proton-coupled electron-transfer (PCET) processes and the occurrence of detrimental side-reactions, thus defining precise guidelines towards improvement of solar fuel formation.

1 Introduction

The still ongoing deployment of fossil fuel resources is causing severe environmental issues such as global warming and climate change.[1,2] The quest for carbon-neutral energy transformations is thus of pivotal importance towards the sustainable development of the whole of humankind. Within this context, the water splitting reaction leading to the generation of oxygen and hydrogen (eqn (1)) represents an ideal, yet challenging, reaction scheme. Hydrogen is indeed a powerful fuel, whose consumption to attain energy only leads to water as the by-product.[3] The main drawback of this reaction is, however, connected to the intrinsic slowness of the single half-reactions (eqn (2) and (3)) which stems from the large kinetic barriers associated with their multi-electronic and multi-protonic reaction mechanism. For these reasons, specific catalyst units, one for the oxidative and one for the reductive side, are required to mediate the conversion of the water substrate into its high energetic constituents.[4,5]

$$2H_2O \rightarrow 2H_2 + O_2 \quad (1)$$

$$2H_2O \rightarrow O_2 + 4H^+ + 4e^- \quad (2)$$

$$2H^+ + 2e^- \rightarrow H_2 \quad (3)$$

[a] Department of Chemical, Pharmaceutical and Agricultural Sciences, University of Ferrara, Via L. Borsari 46, 44121 Ferrara, Italy. E-mail: mirco.natali@unife.it
[b] Department of Chemical Sciences, University of Padova, Via F. Marzolo 1, 35131 Padova, Italy. E-mail: andrea.sartorel@unipd.it

Inspiration for catalyst design can come from the detailed analysis of the same catalytic routines accomplished in biological systems. Water oxidation to dioxygen (*viz.* the oxygen evolving reaction, OER) is indeed performed by plants and cyanobacteria by exploiting a Mn_4CaO_5 cluster (Fig. 1A) which is capable of stepwise storing four oxidizing equivalent (holes), upon photoexcitation of the reaction centre, *via* multiple proton-coupled electron transfer (PCET) processes with the eventual release of molecular oxygen.[6,7] Following Nature's design concept, many artificial molecular catalysts have been reported to date, all sharing a common mechanistic behaviour, as schematized in Fig. 1B.[4] Within this reaction scheme, a key step is represented by the formation of the O–O bond which can occur either by the nucleophilic attack of water to a high-valent metal–oxo intermediate (WNA) or by radical coupling between two metal–oxo species (for artificial catalysts, this is known as the interaction of two metal–oxo units, I2M mechanism).[4]

On the other hand, water reduction to dihydrogen (*viz.* the hydrogen evolving reaction, HER) is performed by certain bacteria by exploiting specific enzymes called hydrogenases.[8] Their active sites are constituted by metal-based cofactors undergoing two consecutive reductions while mediating formation of the H–H bond through proton binding. In Fig. 2A, the metal cofactor of FeFe hydrogenases is depicted as an example, showing the redox active metal centres and the amine proton relay assisting proton binding at the catalytic platform. Even for the HER, several molecular catalysts have been reported in the last years,[9] whose reaction mechanism can be generalized according to the schematic picture in Fig. 2B. Within this reaction, formation of the H–H bond is expected to take place either by protonation of a metal-hydride intermediates (heterolytic mechanism) or by homolysis of two metal-hydrides (homolytic mechanism).[10]

Besides being complicated from the kinetic aspect, the water splitting reaction is also thermodynamically up-hill and an external energy

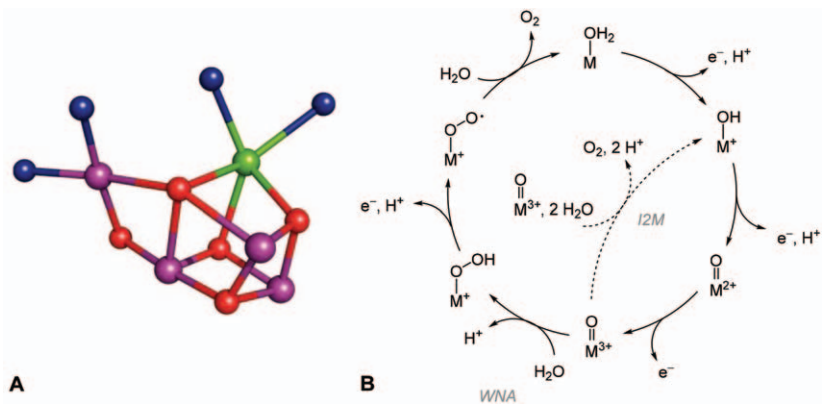

Fig. 1 (A) Structure of the Mn_4CaO_5 oxygen evolving complex (purple = Mn, green = Ca, red = O, blue = OH_2) and (B) general catalytic mechanism for the OER (M is a redox-active metal centre) showing the WNA (full arrows) and I2M (dashed arrows) pathways for O–O bond formation.

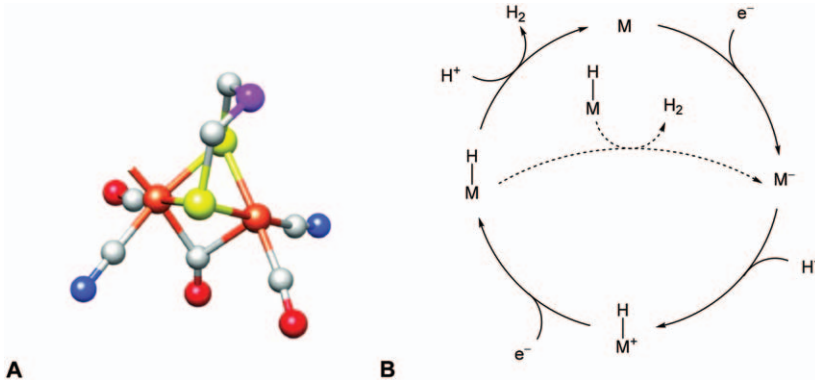

Fig. 2 (A) Structure of the Active site of FeFe hydrogenase (orange = Fe, white = C, yellow = S, red = O, blue = N, violet = NH) and (B) general catalytic mechanism for proton reduction to dihydrogen (M is a redox-active metal centre) showing the heterolytic (full arrows) and homolytic (dashed arrows) pathways for H–H bond formation.

stimulus is thus required. Light can be employed as a powerful tool to promote such a reaction, which may give the possibility to take advantage of an inexhaustible energy source like sunlight. Following these considerations, this work will address light-driven water splitting using molecular species in homogeneous conditions. We will first introduce the basis of this approach and the use of sacrificial cycles, then we will take a look at the experimental aspects by examining (i) the key performance indicators of light-driven catalysis and (ii) the application of optical spectroscopic studies to the evaluation of the efficiency of the process. Finally, we will describe some relevant case studies related with both water oxidation and hydrogen evolution where spectroscopic techniques have been profitably employed to follow the reaction mechanism and guide the identification of the experimental conditions for optimization of the light-driven catalytic process.

2 Light-driven catalysis

Light-driven catalysis of water splitting requires the suitable coupling of photochemical and catalytic components as depicted in Fig. 3A. Within this system, light absorption by the sensitizer (PS) triggers a sequence of electron transfer processes involving an electron donor (D) and an acceptor (A) species leading to charge separation. At this stage, appropriate catalyst units (*viz.* the hydrogen evolving catalyst, HEC, and the oxygen evolving catalyst, OEC) undergo stepwise accumulation of the photogenerated electrons (reduction) and holes (oxidation), respectively, in order to drive the catalytic conversion of the water substrate into products (H_2 and O_2). Notably, one of the most critical tasks within this photoreaction mechanism is the proper synchronization of the light (charge separation) and dark (catalytic) processes. As a matter of fact, photoinduced processes are intrinsically rapid, being associated with fast, single electron transfer (SET) events. On the other hand, catalytic reactions are multi-electronic in nature, involve chemical steps, and are thus slow. Furthermore, the profitable coupling of two light-driven

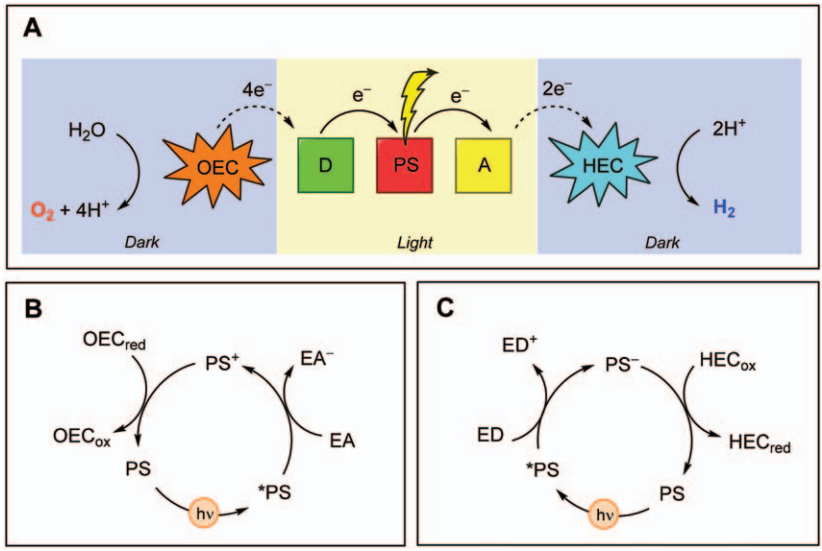

Fig. 3 (A) Schematic representation of a photochemical system for water splitting with indication of both light and dark reactions, (B) oxidative half-reaction with an electron acceptor and (C) reductive half-reaction with an electron donor. Abbreviations: PS = sensitizer, D = donor, A = acceptor, OEC = oxygen evolving catalyst, HEC = hydrogen evolving catalyst, EA = electron acceptor, ED = electron donor.

half-reactions requires that both catalytic processes run at comparable rates so that excessive accumulation of either reducing or oxidizing equivalents is avoided. According to these considerations, optimization of single catalytic half-reactions needs to be primarily envisioned. This can be made by taking advantage of sacrificial reactants, *i.e.*, molecular species that are subjected to decomposition upon electron transfer.[11] For the oxidative half-reaction (Fig. 3B), the minimum set of components is represented by a sensitizer (PS), a catalyst (OEC), and a sacrificial electron acceptor (EA). In this case, excitation of the PS results in oxidative electron transfer quenching by the EA. The photogenerated PS^+ species then acts as the one-electron oxidant towards the OEC which, after accumulation of four oxidizing equivalents, can promote the oxidation of water to dioxygen. Concurrently, for the reductive half-reaction (Fig. 3C), the minimum set of components is composed of a photosensitizer (PS), responsible for light-harvesting, a catalyst (HEC), and an electron donor (ED). Within this three-component system, excitation of the PS is followed by reductive electron transfer quenching by the ED. The photogenerated PS^- species then undergoes electron transfer to the HEC and, by repeating this reaction sequence a second time, two electrons can be stored on the HEC thus resulting in hydrogen evolution.

2.1 Key performance indicators in light-driven catalysis

As previously noticed, optimization of catalytic half-reactions can be profitably performed using sacrificial reactants according to the reaction schemes shown in Fig. 3B and C. These experiments are conducted under

homogeneous conditions in aqueous or organic/aqueous mixtures upon irradiation of solutions containing known amounts of PS, EA or ED for water oxidation or reduction, respectively, and catalyst (OEC or HEC, respectively). The results of these experimental assays typically report the amount of product formed (either oxygen or hydrogen), measured by gas chromatography or by specific sensors, as a function of the irradiation time. Inspection of the resulting kinetic trace allows to attain key performance indicators of the photochemical system examined.[12] One relevant descriptor of the photochemical performance is the maximum amount of product formed at plateau (n_{max}/mol). From this quantity, according to eqn (4), where n_{cat} are the moles of catalyst in the photolyzed solution, it is possible to estimate the maximum turnover number (TON) that quantifies the number of catalytic cycles accomplished per molecule of catalyst.

$$\mathrm{TON} = \frac{n_{max}}{n_{cat}} \tag{4}$$

It should be highlighted that this quantity is commonly employed as a general metric to characterize the efficiency of the light-driven reaction, but this is an erroneous consideration since, as per its definition (eqn (4)), the maximum TON is independent of the irradiation time considered. On the other hand, the TON should be better regarded as a parameter that mainly describes the stability of the photochemical system. As a matter of fact, both PS and catalyst degradation are usually responsible for the levelling-off of product formation and thus are expected to determine the resulting TON value. It should be also pointed out that, still as per its definition (eqn (4)), high TONs are usually achieved at low catalyst concentrations and this evidence should be taken into account when TON is used as the sole metric of the activity of a catalyst in light-driven experiments.

A second relevant quantity that can be extracted from the kinetic trace is the initial rate of product formation (r/mol s^{-1}), usually calculated from the slope in the linear portion of the kinetics. Differently from n_{max} and the resulting TON (see above), this quantity is intrinsically related to the efficiency of the photochemical reaction. As a matter of fact, the initial rate r can be profitably employed to establish the quantum yield (Φ) of the reaction, according to eqn (5) where θ is the absorbed photon flux (Einstein s^{-1}). Typically, instead of the quantum yield, a related parameter called quantum efficiency (QE) is provided, defined according to eqn (6) where z is a numerical factor that takes into account the stoichiometry of the light-driven reaction (*viz.* the photons required to yield one product molecule). Furthermore, according to eqn (7), it is also possible to estimate the turnover frequency (TOF/s^{-1}) defined as the number of catalytic cycles per molecule of catalyst and unit of time. Akin to the TON, this latter quantity depends on the catalyst concentration and thus cannot be employed to univocally assess the activity of a light-driven catalytic reaction.

$$\Phi = \frac{r}{\theta} \tag{5}$$

$$\mathrm{QE} = \frac{z \cdot r}{\theta} \tag{6}$$

$$\mathrm{TOF} = \frac{r}{n_{\mathrm{cat}}} \tag{7}$$

2.2 Optical spectroscopy in light-driven catalysis

The quantum yield of a photochemical reaction (eqn (5)), or its derived parameter QE (eqn (6)), directly depends on the efficiencies of the single events jointly partaking in the whole photochemical process. The detailed evaluation of such kinetic parameters appears of pivotal importance for the optimization of the catalytic routine and for the identification of the experimental conditions where light-driven catalysis can be effectively operative. Considering the reaction schemes in Fig. 3B and C, the quantum yield can be defined according to eqn (8), where η_{light} and η_{dark} are the efficiencies of the light-driven and dark reactions, respectively. The first term η_{light} can be then expressed according to eqn (9), where η_{q} is the efficiency of the oxidative (or reductive) excited state quenching of *PS by EA (or ED) and η_{ce} is the associated cage escape yield. On the other hand, the dark term η_{dark} can be described according to eqn (10), where $\eta_{\mathrm{et},i}$ is the efficiency of the electron transfer process between the photogenerated oxidant/reductant and the *i*-th state of the catalyst (*i.e.*, its pristine and oxidized/reduced forms) and η_{cat} represents the efficiency of the chemical steps involved in the catalytic reaction.

$$\Phi = \eta_{\mathrm{light}} \cdot \eta_{\mathrm{dark}} \tag{8}$$

$$\eta_{\mathrm{light}} = \eta_{\mathrm{q}} \cdot \eta_{\mathrm{ce}} \tag{9}$$

$$\eta_{\mathrm{dark}} = \prod_{i} \eta_{\mathrm{et},i} \cdot \eta_{\mathrm{cat}} \tag{10}$$

Both stationary and time-resolved absorption and emission spectroscopy techniques are of fundamental importance in photochemistry and can be employed as precious tools to estimate either the efficiency terms in eqn (8)–(10) or related kinetic parameters. In particular, η_{q} can be profitably extracted by steady-state luminescence measurements comparing the emission spectra of the PS in the presence and in the absence of the sacrificial agent (EA or ED), according to eqn (11) where F and F_0 are the integrated intensities of the corresponding emission spectra (see Fig. 4A for the estimate of the quenching yield of the reaction of excited $^*[\mathrm{Ru(bpy)_3}]^{2+}$, where bpy = 2,2′-bipyridine, with 0.1 M ascorbate electron donor).

$$\eta_{\mathrm{q}} = 1 - \frac{F}{F_0} \tag{11}$$

η_{ce} can be instead calculated from transient absorption spectroscopy measurements, according to eqn (12), from the ratio of the transient signal of the photogenerated oxidant or reductant ($\Delta\mathrm{OD}_{\mathrm{exp}}$) and that

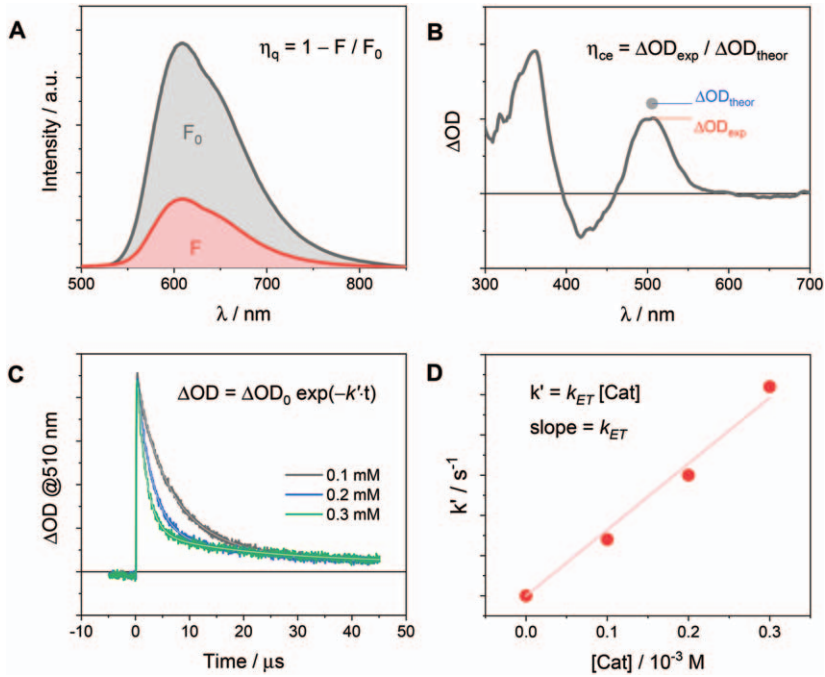

Fig. 4 (A) Comparison of luminescence spectra of $[Ru(bpy)_3]^{2+}$ in the absence (black) and presence (red) of 0.1 M ascorbate at pH 5, (B) transient absorption spectrum of photogenerated $[Ru(bpy)_3]^{+}$ measured by laser flash photolysis and comparison with the theoretical spectrum predicted by quenching yield and actinometry; (C) kinetic traces at 510 nm measured by laser flash photolysis associated with the decay of photogenerated $[Ru(bpy)_3]^{+}$ in the presence of increasing amounts of catalyst; (D) plot of the observed rate (k') *vs.* catalyst concentration for the estimation of k_{ET}.

theoretically expected based on quenching yield (ΔOD_{theor}), with the latter being accurately estimated *via* actinometry. Both ΔOD values are indeed related to the quantity of photogenerated species according to the Lambert–Beer law (eqn (13)), where $\Delta\varepsilon$ ($M^{-1}\,cm^{-1}$) and l (cm) are the difference of attenuation coefficient and optical path, respectively. In Fig. 4B it is reported, as an example, the transient absorption signal of the $[Ru(bpy)_3]^{+}$ reducing agent, photogenerated by reductive quenching of the excited PS with 0.1 M ascorbate, from which the cage escape yield can be determined.

$$\eta_{ce} = \frac{\Delta OD_{exp}}{\Delta OD_{theor}} \tag{12}$$

$$\Delta OD = \Delta\varepsilon \cdot l \cdot c \tag{13}$$

Finally, transient absorption spectroscopy measurements can be employed to estimate the bimolecular rate constant (k_{ET}) of the electron transfer process between the photogenerated oxidant/reductant and the catalyst. These experiments can be easily performed for the first electron transfer process involving the pristine form of the catalyst, but can be in principle applied also for oxidized (or reduced) forms of the catalysts provided that preliminary oxidation (or reduction), *e.g.*, by chemical

means, is considered.[13] In these experiments, pulsed excitation is used to generate a given amount of oxidant (or reductant) by photoreaction with the EA (or ED). Such photogenerated species is detected by its characteristic transient absorption and its decay followed in the presence of variable concentrations of catalyst. The bimolecular rate constant can be thus calculated under pseudo-first order kinetic conditions (*i.e.*, [catalyst] ≫ [oxidant/reductant]), where the decay kinetics of the photogenerated oxidant/reductant depends linearly on the concentration of the catalyst. In Fig. 4C it is reported an exemplar of kinetic traces associated with the decay of the transient signal of the $[Ru(bpy)_3]^+$ reducing agent, photogenerated by reductive quenching of the excited PS with 0.1 M ascorbate, in the presence of increasing amounts of a cobalt polypyridine HEC.[14] Fitting of the kinetic traces using an exponential function provides the pseudo-first order rates (k') from which the bimolecular rate constant k_{ET} can be calculated (Fig. 4D). In principle, this value is of great relevance since it allows for a quantitative determination of the efficiency term $\eta_{et,i}$ according to eqn (14), where Cat_i is the i-th state of the catalyst and k_d is a global rate constant associated with deactivation routes of the photogenerated oxidant/reductant. Since the actual value of k_d is, however, difficult to know, no exact estimate of $\eta_{et,i}$ can be generally attained.

$$\eta_{et,i} = \frac{k_{ET,i}[Cat_i]}{k_{ET,i}[Cat_i] + k_d} \quad (14)$$

Nevertheless, the value of the k_{ET} may give some qualitative insight as to the competition between the forward electron transfer processes involving the catalyst (eventually leading to product formation) and the parallel degradation pathways of the sensitizer. As a matter of fact, the faster the electron transfer the more efficient is the overall photochemical reaction. Not only, evaluation of the bimolecular rate constant k_{ET} under diverse experimental conditions (*e.g.*, different pH, different solvent, different buffer composition or concentration, *etc.*) may also give important information on the mechanism of catalyst activation, pointing out, *e.g.*, the occurrence of PCET processes.[15]

As a final remark, we should remember that all the light-driven and dark processes associated with solar fuel formation within the three-component systems reported in Fig. 3B and C are bimolecular in nature. Accordingly, the concentration of reactants plays a crucial role in quantitatively dictating the overall quantum yield Φ (eqn (8)), as expected based upon the dynamic nature of the electron transfer processes. However, we should not forget that, in some cases, supramolecular interactions may occur between sensitizers and catalysts thus leading to pre-association in solution. Within these assemblies, static quenching events may in principle take place and affect the efficiency of the photoreaction, *e.g.*, by limiting the yield of photogenerated oxidant/reductant (eqn (9)). Hence, steady-state absorption and emission spectroscopy, in combination with other common techniques such as NMR, conductometry (for ion-pairing interactions), *etc.*, can be profitably employed

to assess the potential formation of supramolecular species, to estimate association constants, and to identify proper experimental conditions where these side-phenomena can be avoided. Furthermore, transient absorption spectroscopy in the ultrafast time-regime can be used to follow the quenching dynamics, thus providing a detailed mechanistic insight into these potential side-reactions.

3 Case studies

3.1 Light-driven catalysis of water oxidation (oxygen evolution reaction)

In natural photosynthesis, light driven water oxidation is the process that feeds with reducing equivalents the production of glucose from CO_2. The same concept is transposed to artificial photosynthetic systems, where the pervasive water oxidation routine feeds the reductive counterpart, involving reduction of protons, CO_2 or N_2.[16] Taking inspiration from the natural system, the water oxidation catalyst is coupled with a photosensitizer and a primary electron acceptor. Concerning the photosensitizer, most literature reports took advantage of $[Ru(bpy)_3]^{2+}$ which is characterised by peculiar electrochemical and photochemical properties that make it suitable for both oxidative and reductive photochemical cycles (Fig. 3B and C). In aqueous environment, its oxidation is metal centred and involves the $[Ru^{III}(bpy)_3]^{3+}/[Ru^{II}(bpy)_3]^{2+}$ couple characterised by a redox potential of 1.26 V *vs.* the normal hydrogen electrode (NHE). Its primary reduction is ligand based, associated to the $[Ru^{II}(bpy)_3]^{3+}/[Ru^{II}(bpy^{\bullet-})(bpy)_2]^{+}$ couple characterised by a potential of −1.28 *vs.* NHE.[17,18] The photochemical properties of $[Ru^{II}(bpy)_3]^{2+}$ are associated to a metal to ligand charge transfer (MLCT) band centred at 450 nm ($\varepsilon = 14\,000\ M^{-1}\,cm^{-1}$). Upon excitation, a triplet excited state manifold $*[Ru^{III}(bpy^{\bullet-})(bpy)_2]^{2+}$ (further abbreviated as $*[Ru^{II}(bpy)_3]^{2+}$) is generated, having an energy of 2.12 eV and a lifetime of 580 ns in deaerated aqueous solution.[19] The combination of the redox and photochemical properties of the ground state allows the estimation of the redox potentials of the excited state $E([Ru^{III}(bpy)_3]^{3+}/*[Ru^{II}(bpy)_3]^{2+}) = -0.86$ V *vs.* NHE and $E(*[Ru^{II}(bpy)_3]^{2+}/[Ru^{II}(bpy^{\bullet-})(bpy)_2]^{+}) = +0.84$ V *vs.* NHE.[20] In particular, photochemical cycles for water oxidation take advantage of the photogeneration of the $[Ru^{III}(bpy)_3]^{3+}$ oxidant in the presence of suitable electron acceptors, with the persulfate anion $S_2O_8^{2-}$ being frequently exploited. Upon light absorption, the excited state $*[Ru^{II}(bpy)_3]^{2+}$ is oxidized by the persulfate anion $S_2O_8^{2-}$ to $[Ru^{III}(bpy)_3]^{3+}$. The reduced $S_2O_8^{3-}$ undergoes a homolytic O–O bond cleavage producing a sulfate dianion (SO_4^{2-}) and a sulfate radical anion ($SO_4^{\bullet-}$), this latter is a powerful oxidant ($E(SO_4^{\bullet-}/SO_4^{2-})$ estimated as +3.4 V *vs.* NHE) and oxidizes a second molecule of $[Ru^{II}(bpy)_3]^{2+}$ to $[Ru^{III}(bpy)_3]^{3+}$. As such, one absorbed photon generates two equivalents of $[Ru^{III}(bpy)_3]^{3+}$ and indeed the quantum yield for $[Ru^{III}(bpy)_3]^{3+}$ generation is 2.[21] The case studies that we present in this paragraph deal with the combination of the $[Ru(bpy)_3]^{2+}/S_2O_8^{2-}$ photosensitizer/acceptor couple with water oxidation catalysts, focusing in particular on the mechanistic aspects.

3.1.1 The tetraruthenium polyoxometalate $\{Ru^{IV}(H_2O)_4(\mu\text{-}OH)_2(\mu\text{-}O)_4[\gamma\text{-}SiW_{10}O_{36}]\}^{10-}$. The $\{Ru^{IV}(H_2O)_4(\mu\text{-}OH)_2(\mu\text{-}O)_4[\gamma\text{-}SiW_{10}O_{36}]\}^{10-}$ (**RuPOM**) WOC (Fig. 5) was independently reported in 2008 by the groups of Prof. Bonchio[22] and Prof. Hill.[23] Its structure revealed two 90° staggered $\gamma\text{-}SiW_{10}O_{36}^{8-}$ polyoxometalate inorganic ligands coordinating a $[Ru_4(\mu\text{-}O)_4(\mu\text{-}OH)_2(H_2O)_4]^{6+}$ central core, in an overall D_{2d} symmetry. This tetraruthenate core is reminiscent of the Mn_4-oxo core of the natural oxygen evolving centre, but can also be considered an optimized fragment of ruthenium oxide, where all the metal centres are available for water binding: a fragment of a ruthenium oxide embedded in the polyoxometalate molecular metal oxide. A further analogy between **RuPOM** and ruthenium oxide emerges when considering the reactivity in water oxidation catalysis. The tetraruthenate core in **RuPOM** displays redox reactivity in water solution (pH 0.6–12), with an experimental evidence of up to nine redox states, with ruthenium centres spanning from oxidation states III to V.[24] The associated redox transformations are affected by the pH and by the electrolyte, but are typically monoelectronic and associated to a proton transfer; thus, they occur in a narrow potential range, where consecutive events are separated by 0.1–0.25 V.[24] This property enables the redox potential levelling and the generation of Ru(VI) highly oxidized intermediates achieving oxidation of water to oxygen at low overpotential (0.25–0.35 V).[25] The activity of **RuPOM** in combination with the light activated $[Ru(bpy)_3]^{2+}/S_2O_8^{2-}$ system was reported by the group of Prof. Hill in 2009, irradiating with a Xe lamp (420–520 nm) a solution of 1.0 mM $[Ru(bpy)_3]^{2+}$, 5.0 mM $Na_2S_2O_8$, 5.0 μM **RuPOM** in 20 mM phosphate buffer, pH 7.2. Oxygen was formed quickly and last *ca.* 30 minutes. Key performance indicators of the system were: (i) a QE of 9%; (ii) an oxygen yield of 38% based on

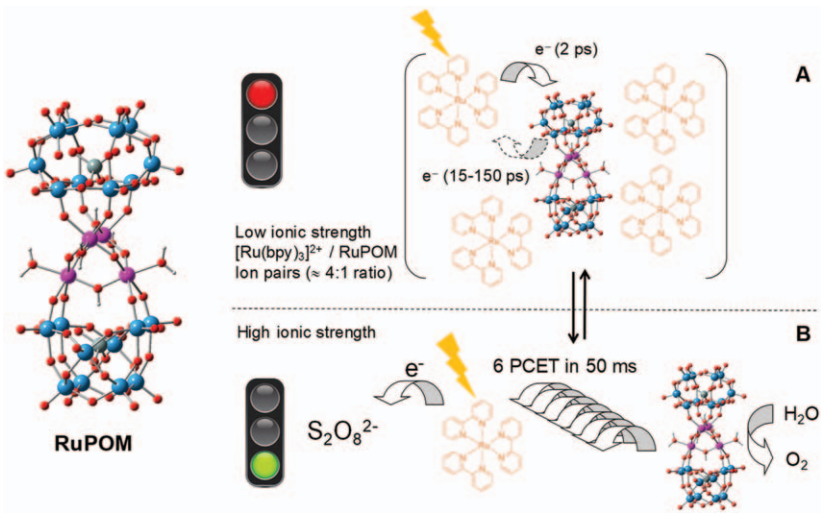

Fig. 5 Structure of **RuPOM**, (A) formation of $[Ru(bpy)_3]^{2+}$/**RuPOM** ion pairs under low ionic strength conditions, where oxidative quenching of $*[Ru(bpy)_3]^{2+}$ occurs in 2 ps, followed by charge recombination in 15–150 ps; (B) under high ionic strength conditions, photochemical oxidation of $*[Ru(bpy)_3]^{2+}$ by $S_2O_8^{2-}$ occurs, with $[Ru(bpy)_3]^{3+}$ feeding **RuPOM** up to water oxidation.

persulfate consumption; (iii) TON in the range 180–350; (iv) TOF of $\sim 8 \times 10^{-2}$ s^{-1}. From the optimised conditions above, it is clear that the oxygenic performance requires [**RuPOM**] ≪ [[$Ru(bpy)_3$]$^{2+}$]. Indeed, at higher concentrations of **RuPOM** ion pairs form between the dicationic photosensitizer and the decaanionic **RuPOM** catalyst; spectroscopic and conductometric titration show an average 4 : 1 [$Ru(bpy)_3$]$^{2+}$: **RuPOM** ratio in globular and porous aggregates.[26,27] The photochemical investigation of such aggregates by ultrafast spectroscopy indicates a deactivation of the *[$Ru(bpy)_3$]$^{2+}$ excited state by ultrafast oxidative electron transfer with **RuPOM** (2 ps), followed by charge recombination (15–150 ps) (Fig. 5). In short, the evident outcome of the ultrafast spectroscopy is that the [$Ru(bpy)_3$]$^{2+}$/**RuPOM** ion pairs are inactive towards photochemical water oxidation, since they lead to a fast quenching of the excited sensitizer while driving the electron flow in the undesired, opposite way. This is one drawback of the [$Ru(bpy)_3$]$^{2+}$/**RuPOM** combination that contributed to hamper the development of efficient photoanodes.[28,29]

In aqueous solution, the prevention of ion pair formation can be accomplished by lowering the concentrations of **RuPOM** or by increasing ionic strength (by means of buffer and/or electrolytes, Fig. 5). Following these expedients, photochemical generation of [$Ru^{III}(bpy)_3$]$^{3+}$ proceeds smoothly and [$Ru^{III}(bpy)_3$]$^{3+}$ further feeds the **RuPOM** with oxidising equivalents in the cycle that leads to oxygen evolution. In particular, the reaction of [$Ru^{III}(bpy)_3$]$^{3+}$ with **RuPOM** can be followed through laser flash photolysis, monitoring the bleach recovery at 450 nm characteristic of the regeneration of [$Ru^{II}(bpy)_3$]$^{3+}$ by oxidation of the catalyst (Fig. 3C). Under pseudo first-order conditions (*i.e.*, [[$Ru^{III}(bpy)_3$]$^{3+}$] ≪ [**RuPOM**]) the bleach recovery shows a clear dependence on **RuPOM** concentration and monoexponential fittings of the traces can provide the bimolecular rate constant for electron transfer.[30] The Marcus model for bimolecular electron transfer foresees the formation of the encounter complex (eqn (15)), electron transfer to give the successor complex (eqn (16)), product diffusion (eqn (17)). The bimolecular rate constant can be derived as in eqn (18), considering a stationary state for both the encounter and successor complexes.

$$[Ru(bpy)_3]^{3+} + \mathbf{RuPOM} \rightleftharpoons \{[Ru(bpy)_3]^{3+} \cdot \mathbf{RuPOM}\},\ k_1,\ k_{-1} \quad (15)$$

$$\{[Ru(bpy)_3]^{3+} \cdot \mathbf{RuPOM}\} \rightleftharpoons \{[Ru(bpy)_3]^{2+} \cdot \mathbf{RuPOM}^{ox}\},\ k_2,\ k_{-2} \quad (16)$$

$$\{[Ru(bpy)_3]^{2+} \cdot \mathbf{RuPOM}^{ox}\} \rightarrow [Ru(bpy)_3]^{2+} + \mathbf{RuPOM}^{ox},\ k_3 \quad (17)$$

$$k_I = \frac{k_1}{[1 + (1 + k_{-2}/k_3) \times k_{-1}/k_2]} \quad (18)$$

For [$Ru^{III}(bpy)_3$]$^{3+}$ and **RuPOM** partners, the rate constant k_I falls in the diffusion limit in the pH range 2–7 and is independent of the buffer concentration. A diffusion limited rate is observed when both $k_3 \gg k_{-2}$ and $k_2 \gg k_{-1}$ conditions are satisfied, in which case $k_I \approx k_1$: this is

beneficial towards the accumulation of the first oxidation equivalent in **RuPOM**^{OX} (*i.e.*, the backward processes do not significantly compete with the forward processes in eqn (15)–(17)).

Another striking feature of **RuPOM** WOC is that its productive, sequential oxidation by $[Ru^{III}(bpy)_3]^{3+}$ to highly oxidised intermediates is also very fast. This can still be verified by laser flash photolysis, operating with $[\mathbf{RuPOM}] \ll [Ru^{III}(bpy)_3]^{3+}$.[26] Indeed, at low **RuPOM** catalyst concentrations (in the range of μM), the amount of $[Ru^{III}(bpy)_3]^{3+}$ being reduced within the time window of the laser flash photolysis experiment (*ca.* 50 ms) exceeds up to 6 times the amount of **RuPOM**,[30] meaning that in this timescale **RuPOM** is oxidised up to a Ru(VI) di-oxo intermediate that was postulated to be involved in the water nucleophilic attack for the construction of the O–O bond (Fig. 6).[25] Since the sequential oxidation of **RuPOM** involves the evolution of Ru(IV)–OH_2→Ru(V)–OH→Ru(VI)–O moieties, according to PCET mechanisms, we have recently investigated the effect of the aqueous buffer composition and concentration on the kinetics of the oxidation of **RuPOM** by $[Ru^{III}(bpy)_3]^{3+}$.

A visual inspection of the kinetic traces (Fig. 6A) suggests a beneficial effect in the bleach recovery by increasing the concentration of the buffer: the ΔOD recovery indicates the occurrence of up to 6 PCET events from **RuPOM**, with the HPO_4^{2-} base of the buffer being responsible for the transfer of the protons, while electrons are conveyed to $[Ru^{III}(bpy)_3]^{3+}$. The profile of the ΔOD recovery in Fig. 6A, associated with the

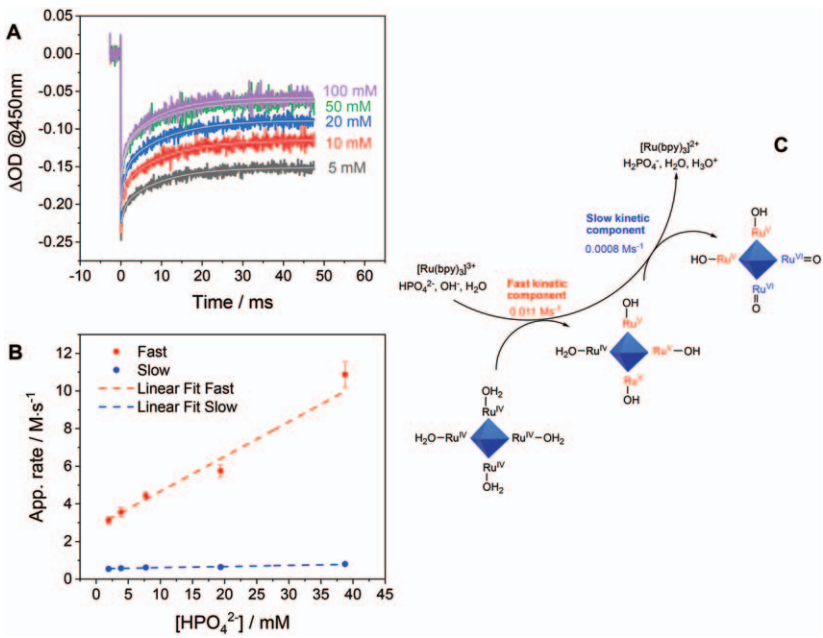

Fig. 6 (A) kinetic traces at 450 nm obtained by laser flash photolysis of 100 μM $[Ru(bpy)_3]Cl_2$, 5 mM $Na_2S_2O_8$, 2.5 μM Na_{10}**RuPOM**, 0.1 M Na_2SO_4 in unbuffered water and in 5–100 mM phosphate buffer at pH 7.0. (B) Plot of apparent rates for $[Ru(bpy)_3]^{3+}$ consumption *vs.* the concentration of base. (C) Schematic representation of the accumulation of oxidation equivalents on **RuPOM** through sequential PCET. Adapted from ref. 30 with permission from the Royal Society of Chemistry.

$[Ru(bpy)_3]^{3+} \rightarrow [Ru(bpy)_3]^{2+}$ conversion, can be used to extract kinetic parameters: the traces can be indeed fitted with bi-exponential functions to describe the recovery of the ΔOD along the experiments. From the fitting parameters, two apparent rates for the reactivity of $[Ru(bpy)_3]^{3+}$ with **RuPOM** due to the fast and slow components can be derived. The plot of the apparent rates *versus* the concentration of HPO_4^{2-} base show a linear dependence supporting a first-order dependence in $[HPO_4^{2-}]$ of both apparent rates (Fig. 6B),[30] confirming the role of the base in assisting the removal of the protons from **RuPOM** along its conversion to high oxidized states through reactivity with $[Ru(bpy)_3]^{3+}$ (Fig. 6C). The effect of HPO_4^{2-} base associated with the PCET mechanism of **RuPOM** impacts the O_2 evolution of the system. The initial rate of O_2 evolution show an initial increase upon increase of buffer concentration highlighting the beneficial effect of the buffer in accelerating the PCET events. However, a further increase of buffer concentration in the reaction conditions leads to a progressive abatement of the activity. This effect is ascribed to a rapid degradation of the $[Ru(bpy)_3]^{2+}$ photosensitizer as revealed by UV-Vis analysis of the reaction solution, which visibly turns from brilliant orange to brownish along the first minutes of irradiation.[31]

3.1.2 Cobalt polyoxometalates. Cobalt catalysts has gained interest since the seminal work of Kanan and Nocera on the electrodeposited, self-healing cobalt oxide/phosphate (CoPi) catalytic material.[32] Many efforts were dedicated to the investigation of photochemical cycles involving cobalt coordination compounds with organic ligands,[33,34] cobalt based polyoxometalates,[35] and cobalt oxide materials in the form of nanoparticles.[36,37] In this paragraph, we focus on a couple of examples of cobalt based polyoxometalates investigated in the $[Ru(bpy)_3]^{2+}/S_2O_8^{2-}$ system. The reason for this choice is associated with the fact that polyoxometalates promote the coordination of small cobalt oxo cluster with a molecular definition. Being polyanionic, the same precautions previously discussed for **RuPOM** to avoid the formation of unproductive ion pairs with $[Ru(bpy)_3]^{2+}$ photosensitiser should be considered. One further point that needs to be considered in cobalt polyoxometalate chemistry is the partial release of Co(II) ions in aqueous solution, that may lead to the degradation of the parent POM and to the formation of active, POM-free metal oxides as the real catalysts.[38,39] One case is $[Co_4(H_2O)_2(\alpha\text{-}PW_9O_{34})_2]^{10-}$ (**Co4POM**, Fig. 7), that was reported in water oxidation catalysis by the Hill group in 2010,[40] employing $[Ru(bpy)_3]^{3+}$ oxidant (under dark conditions), and subsequently implemented in the light driven $[Ru(bpy)_3]^{2+}/S_2O_8^{2-}$ system.[41] The question if $[Co_4(H_2O)_2(\alpha\text{-}PW_9O_{34})_2]^{10-}$ was the actual operating WOC was raised by the group of Finke, who recognised that in aqueous solution **Co4POM** releases Co(II) aqueous ions, that form under electrochemical conditions an active metal oxide at the electrode surface.[39] Concerning homogeneous conditions, the reactivity of **Co4POM** towards $[Ru(bpy)_3]^{3+}$ oxidant was monitored through laser flash photolysis, starting from a stock solution of **Co4POM** in phosphate or borate buffer.[42]

It was observed that the amount and the rate of bleach recovery (associated with the ET from Co–POM to photogenerated $[Ru(bpy)_3]^{3+}$ were

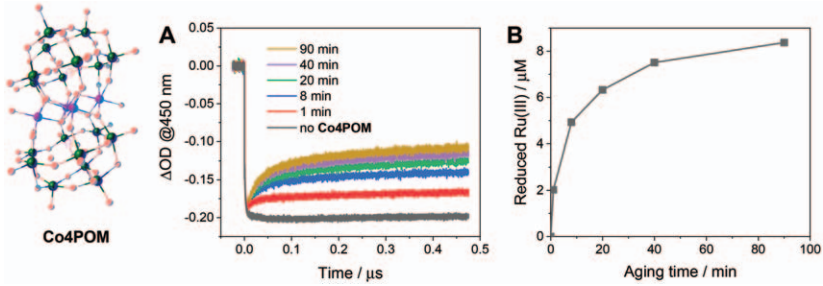

Fig. 7 Structure of $[Co_4(H_2O)_2(\alpha\text{-}PW_9O_{34})_2]^{10-}$ (**Co4POM**). (A) Kinetic traces at 450 nm by laser flash photolysis at different aging times of **Co4POM** (starting from a freshly prepared 1 mM solution in 80 mM phosphate buffer, pH 8) and (B) amount of $[Ru(bpy)_3]^{3+}$ reacting with **Co4POM** in 450 ms timescale, as a function of aging time of the solution of **Co4POM**. Adapted from ref. 42 with permission from the Royal Society of Chemistry.

both increasing with the solution aging, indicating a transformation of the parent Co–polyoxometalate in a more reactive species (Fig. 7). As to the nature of the active species, aqueous Co^{2+} ions were ruled out by control experiments performed with $Co(NO_3)_2$, giving no appreciable reactivity towards $[Ru(bpy)_3]^{3+}$ in this time scale. Therefore, the most likely hypothesis is an earlier decomposition product, possibly a fragment of the original polyoxoanion of 2 : 1 Co : POM stoichiometry.

Thus, further studies on cobalt based polyoxometalates required a preliminary assessment of the stability in the operating conditions. The stability of the Co–POM and the possible release of Co(II) can be evaluated by spectroscopic techniques, *e.g.*, ^{31}P NMR line broadening, or by electrochemical ones.[39] When stability conditions are satisfied, the reactivity of Co–POMs towards $[Ru(bpy)_3]^{3+}$ can be verified by laser flash photolysis. This was the case for some Co–POMs characterised by multinuclear Co-oxo cores, for which two general features emerge for their reactivity with photogenerated $[Ru(bpy)_3]^{3+}$: (i) a diffusional rate constant for the primary electron transfer event ($k > 10^9$ M^{-1} s^{-1}); (ii) the observation of multiple electron transfer events, with up to 2 ET per Co centre. Both these features are productive towards the fast generation of highly oxidised intermediates involved in water oxidation.[43,44] Similarly to the case of ruthenium chemistry discussed above, the oxidative reactivity of cobalt species through $Co^{II/III/IV}$ states foresees the removal of electrons coupled to removal of protons as represented in eqn (19), where the formal Co(IV)–O species can be also described as a Co(III)–$O^{\bullet}$, cobalt oxyl, species.

$$Co^{II}-OH_2 \rightleftharpoons Co^{III}-OH + e^- + H^+ \rightleftharpoons Co^{IV}-O + e^- + H^+ \qquad (19)$$

Therefore, the question on which base manages the proton transfer in the PCET events along the photochemical cycle applies also to cobalt polyoxometalates. This argument was investigated with the $[Co_6(H_2O)_2(\alpha\text{-B-}PW_9O_{34})_2(PW_6O_{26})]^{17-}$ (further abbreviated **Co6POM**, Fig. 8), that displays two symmetrical Co^{II}–OH_2 moieties with a pK_a of 7.6.[45]

The Pourbaix diagram of **Co6POM** for the oxidation of Co^{II} to Co^{III} shows a constant potential region above pH 7.6 (due to oxidation of Co^{II}–OH to

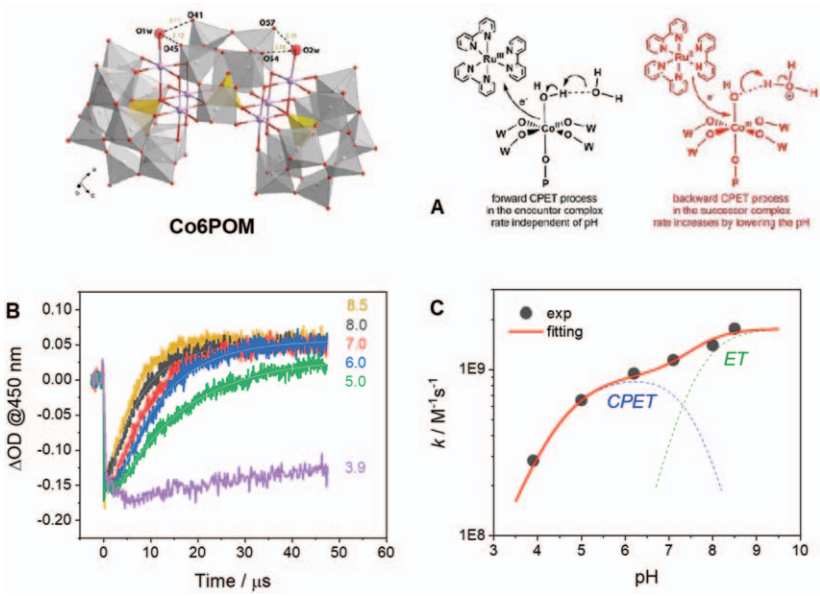

Fig. 8 Structure of $[Co_6(H_2O)_2(\alpha\text{-B-}PW_9O_{34})_2(PW_6O_{26})]^{17-}$ (**Co6POM**), where O1w and O2w are the two oxygen from the water molecules coordinated to Co^{II} centers of the polyoxometalate. (A) Schematic representation of the CPET from Co^{II}–OH_2 in **Co6POM** to $[Ru(bpy)_3]^{3+}$ with hydrogen bonded water acting as a base; (B) kinetic traces at 450 nm obtained by laser flash photolysis of 50 μM $[Ru(bpy)_3]Cl_2$, 5 mM $Na_2S_2O_8$, 100 μM **Co6POM**, 0.1 M Na_2SO_4 and 50 mM buffer at different pH values; (C) plot of the bimolecular rate constant for reactivity of **Co6POM** with $[Ru(bpy)_3]^{3+}$ (in logarithmic scale; black dots are the experimental data) *vs.* pH and related fitting (solid, red trace) considering both contributions from reactivity of Co^{II}–OH_2 (dashed blue line, CPET mechanism) and Co^{II}–OH (dashed green line, ET mechanism) in **Co6POM**. Adapted from ref. 45 with permission from John Wiley & Sons, Copyright 2021 The Authors.

Co^{III}–OH) and a region below pH 7.6 where the potential shows a Nernstian behaviour with a dependence close to 59 mV pH^{-1} unit, indicative of a PCET associated to oxidation of Co^{II}–OH_2 to Co^{III}–OH. Oxidation of **Co6POM** by photogenerated $[Ru^{III}(bpy)_3]^{3+}$ was then investigated by flash photolysis conducted at different pH and the ΔOD recovery traces and the associated bimolecular rate constants showed a clear pH dependence (Fig. 8B), whereas no dependence on the buffer concentration was apparent. While at pH > 7.6 a simple ET process, approaching the diffusion limit, is involved in the oxidation of Co^{II}–OH to Co^{III}–OH, at pH < 7.6 the results are consistent with water being the base responsible for a concerted proton electron transfer (CPET) associated with oxidation of Co^{II}–OH_2 to Co^{III}–OH by $[Ru^{III}(bpy)_3]^{3+}$. This interpretation is supported by the preorganization of water channels at the hydrophilic **Co6POM** surface and engaging hydrogen bonds with the Co^{II}–OH_2 group, as demonstrated by the crystallographic structure. The experimental trend of the bimolecular rate constant *vs.* the pH was fitted with a model considering both CPET and ET processes (whose contribution is associated to the pK_a of 7.6 for the Co^{II}–OH_2/Co^{II}–OH groups, Fig. 8C) and applying the Marcus model described above for **RuPOM** (eqn (15)–(18)). The dependence of the overall k on pH could be surprising at first sight, since forward CPET

processes with water acting as a base should display a pH independent rate constant. Thus, the most plausible explanation for the experimental observation is associated with the increasing competition of the reverse process, namely the backward CPET within the successor complex where H_3O^+ is a reactant (Fig. 8A).[45]

3.2 Light-driven catalysis of hydrogen evolution

3.2.1 Kinetics of the primary photochemical steps. One of the first HECs employed in light-driven cycles which was investigated in details by optical spectroscopy techniques is the dimeric iron complex $[Fe_2(\mu\text{-}Cl_2bdt)(CO)_6]$ (where Cl_2bdt = 3,6-dichlorobenzene-1,2-dithiolate), representing an artificial model of the active site of FeFe hydrogenases.[46] This metal complex leads to hydrogen production upon photoirradiation when combined with $[Ru(bpy)_3]^{2+}$ as the sensitizer and ascorbate as the sacrificial electron donor in 50/50 DMF/H_2O. Under optimized conditions (140 μM catalyst, pH 5.5), hydrogen is produced with a maximum TON of 200 after 2.5 h, with a maximum TOF of 2.7 min^{-1} and a quantum yield (Φ) of 1%. Investigation of the photochemical system by both steady-state and time-resolved spectroscopy revealed important mechanistic information. (i) Photoluminescence quenching experiments show that the excited state of the $[Ru(bpy)_3]^{2+}$ sensitizer does not react with the diiron catalyst while the primary photochemical process is the reductive quenching of $^*[Ru(bpy)_3]^{2+}$ by ascorbate, thus confirming the expected mechanistic pathway of Fig. 3C. (ii) This process occurs with an efficiency of $\eta_q = 96\%$ and leads to an almost quantitative generation of $[Ru(bpy)_3]^{+}$ (*i.e.*, $\eta_{ce} \sim 1$ and $\eta_{light} \sim \eta_q$), as demonstrated by transient absorption spectroscopy measurements. (iii) The one-electron reduction of the catalyst by the photogenerated $[Ru(bpy)_3]^{+}$ species occurs efficiently with a bimolecular rate constant of $1.4 \cdot 10^9$ M^{-1} s^{-1}.

3.2.2 Understanding the role of pH on the light-driven HER. During the last years, parallel studies have involved the identification of alternative compounds as potential HECs. In this regard, the application of transition metal complexes based on cobalt as the metal ion has been extremely intense.[47] The potential activity of cobalt species as HECs under light-driven conditions was first considered by Lehn and coworkers in early eighties of the XX century.[48] Among the plethora of cobalt complexes employed, cobaloximes hold a special place. Starting from these promising results, **CoDMG** (Fig. 9) was subsequently used with a large variety of sensitizers and electron donors. Relevant results were attained using, *e.g.*, a rhenium(I) complex coupled with TEOA (TON = 150 after 9 h and TOF = 0.22 min^{-1}),[49] a platinum complex in combination with TEOA (TON ~ 100 after 10 h at pH 8.5),[50] porphyrin chromophores (TON ~ 28 after 40 h with a zinc(II) porphyrin and TEOA;[51] TON = 117, TOF = 3.6 min^{-1} and a quantum efficiency QE = 9.2% with an aluminium(III) porphyrin and ascorbate)[52] and the Eosin Y dye with TEOA (TON ~ 180 after 20 h and a Φ = 4% under optimized conditions).[53] Interestingly, besides the different performances

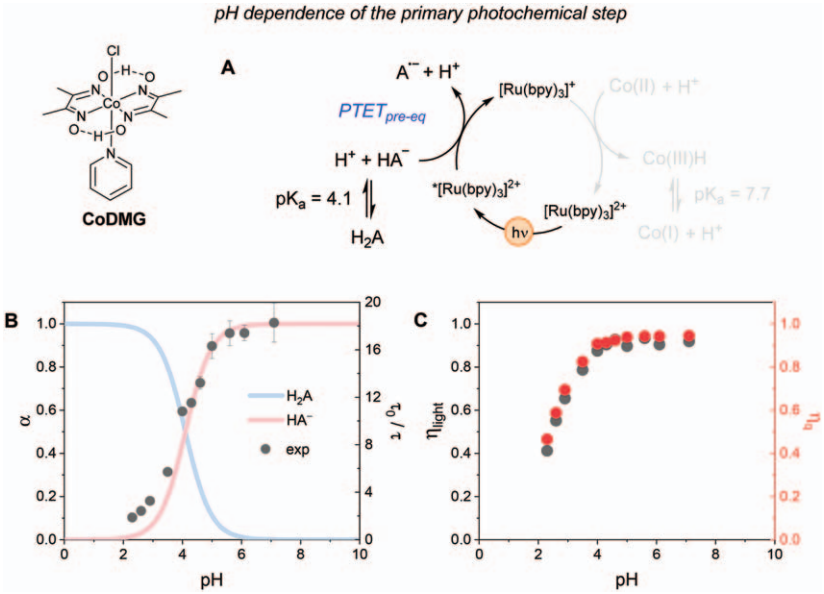

Fig. 9 Molecular structure of **CoDMG** and (A) schematic representation of the pH dependence of the primary photochemical pathway (H_2A = ascorbic acid); (B) trend of the τ_0/τ ratio *vs.* pH for the quenching of $[Ru(bpy)_3]^{2+}$ by ascorbic acid in 50/50 acetonitrile/H_2O; (C) trend of the efficiency terms η_q and η_{light} as a function of the pH (η_q is obtained from the data in Fig. 9B, η_{light} is estimated *via* actinometry from the maximum ΔOD at 510 nm). Adapted from ref. 54 with permission from American Chemical Society, Copyright 2017.

recorded with all the system examined, whose variability mainly stems from the diverse components and experimental conditions used, all the photochemical studies conducted in aqueous mixtures pointed to a relevant role of the pH on the catalytic performances, with a trend displaying a common bell-shaped profile. In order to find a rationale for this issue, a prototype photochemical system involving the cobaloxime **CoDMG** catalyst, $[Ru(bpy)_3]^{2+}$ as the sensitizer and ascorbate as the sacrificial electron donor in 50/50 acetonitrile/H_2O was detailedly studied.[54] For this system, the photochemical hydrogen evolution rate maximizes at pH 5 and decrease at both lower and higher pH values. Once experimentally established that hydrogen photosynthesis by this photochemical system occurs according to the reaction sequence of Fig. 3C,[55] steady-state and time-resolved emission/absorption spectroscopic studies were accomplished to elucidate the role of pH. Within this photoreaction scheme, the primary photochemical process is thus represented by the reductive quenching of the excited $[Ru(bpy)_3]^{2+}$ by the ascorbic acid donor with the concurrent generation of the reduced $[Ru(bpy)_3]^{+}$ species. For this reaction step, emission studies show that the quenching efficiency η_q is strongly pH dependent, wherein the τ_0/τ ratio displays a clear trend that parallels the speciation of the ascorbate anion in solution (Fig. 9B). This is consistent with photogeneration of $[Ru(bpy)_3]^{+}$ occurring through a sequential proton-transfer electron-transfer (PTET) involving a pre-equilibrium kinetics, for which the rate

constant of the process is proportional to the equilibrium constant of the ionization of ascorbic acid.[56] Furthermore, transient absorption spectroscopy measurements show that the formation of the photogenerated $[Ru(bpy)_3]^+$ reductant is almost quantitative upon photoexcitation ($\eta_{ce} \sim 1$, Fig. 9C). Thus, within the photoactivated cycle the progressive increase of the catalytic performance from acidic up to pH 5 can be attributed to the increase in the η_{light} efficiency term (Fig. 9A).

If the increase of the pH is beneficial to improve the yield of photogenerated $[Ru(bpy)_3]^+$ reductant, its pH independence above pH 5 (Fig. 9C) cannot explain the progressive decrease in the light-driven catalytic rates with increasing pH. In order to shine light on this issue, transient absorption experiments were conducted to evaluate the effect of the pH on the dark catalytic step, *i.e.*, the electron transfer process from $[Ru(bpy)_3]^+$ to **CoDMG**. We should highlight that, in these studies, **CoDMG** is present in the form of a cobalt(II) complex with a free coordination site due to reduction by the ascorbate electron donor and removal of the apical chloride ligand.[54] The spectroscopic results showed that at pH 3.2 the absorption spectrum associated with the photogenerated reductant (maximum at 510 nm) decays to the baseline without formation of any other transient signals (Fig. 10B). This spectral changes are consistent with the coupling of the electron transfer to the Co(II) catalyst with protonation, leading to the formation of a Co(III)-hydride, which is known to lack any absorption in the visible.[57] Consistent with this hypothesis, the bimolecular rate constant for this

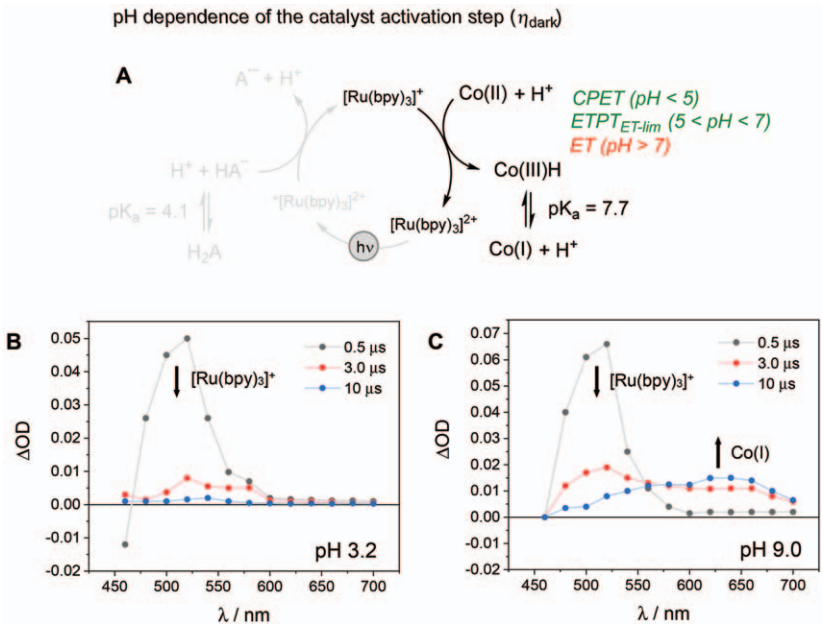

Fig. 10 (A) Schematic representation of the pH dependence of the electron transfer to the catalyst; (B) transient absorption spectra associated with the electron transfer from $[Ru(bpy)_3]^+$ to **CoDMG** at pH 3.2; (C) transient absorption spectra associated with the electron transfer from $[Ru(bpy)_3]^+$ to **CoDMG** at pH 9. Adapted from ref. 54 with permission from American Chemical Society, Copyright 2017.

reaction showed an appreciable pH dependence at pH < 5, suggesting a concerted mechanism of the PCET reaction (CPET).[54] Similar spectral changes as those in Fig. 10B were observed also between pH 5–7, still suggesting formation of Co(III)H upon electron transfer from $[Ru(bpy)_3]^+$ to **CoDMG**. Within this range, however, the rate constant becomes practically pH independent suggesting a switch in the PCET mechanism from CPET to ETPT with a rate limiting ET step.[56] On the other hand, at pH 9 (Fig. 10C) the decay of the absorption at 510 nm is followed by the development of a new transient with maximum at *ca.* 620 nm, attributable to a Co(I) species.[53] This suggests that, under these conditions, electron transfer from $[Ru(bpy)_3]^+$ to **CoDMG** involves a simple electron transfer (ET) reaction. By monitoring the ΔOD at 620 nm as a function of the pH it was possible to determine a $pK_a = 7.7$ for the Co(III)-H deprotonation.[54] Hence, the protonation equilibrium of the Co(I) catalytic intermediate at neutral to basic pH, resulting in a progressively inefficient protonation above pH 5, clearly has an active role in the light-driven catalytic performance of the whole photochemical system (Fig. 10A). Interestingly, similar conclusions were also obtained by Reisner, Durrant and co-workers who investigated the pH effect on the light-driven catalytic performance by a nickel bis(diphosphine) catalyst in combination with $[Ru(bpy)_3]^{2+}$ and ascorbic acid.[58] For this latter, however, the progressive loss in activity in the neutral to basic pH range was mainly associated with the degree of protonation of the pendant amines of the catalyst that are known to serve as proton relays towards the formation of the nickel(II)-hydride catalytic intermediate.[59]

3.2.3 Understanding potential sources of inefficiency in light-driven HER. Although cobaloximes and related molecular analogues such as cobalt diimine-dioxime complexes have received great attention, their extensive application in light-driven catalytic systems has been often hampered due to instability issues and limited-to-negligible activity in fully aqueous environments. For all these reasons, in the last years, cobalt complexes featuring polypyridine chelating ligands have been developed and effectively employed in light-driven catalytic cycles.[47] For instance, in combination with $[Ru(bpy)_3]^{2+}$ as the sensitizer and ascorbic acid as the sacrificial electron donor, maximum TON of 1875, with a TOF of 134 h^{-1} and a QE = 7.5% were achieved with a cobalt complex featuring a tetradentate polypyridine ligand,[60] while still larger performances were attained using cobalt complexes featuring either a pentadentate or a hexadentate amino-polypyridine ligands (maximum TONs of 1600 and 5520, maximum TOFs of 0.4 and 1.4 s^{-1} and quantum efficiencies up to 7 and 11%, respectively).[61–63] For these systems, the light-driven generation of hydrogen should be in principle limited by consumption of the sacrificial electron donor. In practice, it is instead limited by parallel degradation of the chromophore unit.[60] This notwithstanding, a full recovery of the pristine catalytic activity cannot be attained upon simple addition of fresh sensitizer after one full catalytic cycle. As a matter of fact, when using ascorbate as the sacrificial donor, accumulation of dehydroascorbic acid (DHA) occurs following

oxidation and this species can behave as an effective oxidizing agent thus short-circuiting the light-driven catalytic process (Fig. 11A). Experimental evidence of this side reaction was acquired by transient absorption spectroscopy of aqueous solutions of $[Ru(bpy)_3]^{2+}$ sensitizer and ascorbate donor upon addition of increasing aliquots of DHA.[64] As can be seen in Fig. 11B, in the absence of DHA a transient signal develops at 510 nm, characteristic of the reduced $[Ru(bpy)_3]^{+}$ chromophore attained *via* reductive quenching by the ascorbate donor. This transient is appreciably long-lived in a time-scale of 50 μs. In the presence of DHA, on the other hand, the transient absorption at 510 nm decays more rapidly and the decay kinetics appreciably depends on the concentration of added DHA. This suggests that DHA is capable of oxidizing the photogenerated $[Ru(bpy)_3]^{+}$ sensitizer, thus hampering its reactivity towards the electron transfer to the catalyst. Fitting the kinetic traces under pseudo-first order conditions allows to extract the bimolecular rate constant for the reaction of DHA with $[Ru(bpy)_3]^{+}$ (Fig. 11C). Although not intrinsically fast, this side reaction can become efficient when employing highly active catalysts such as polypyridine cobalt complexes since increasingly higher amounts of DHA are generated per hydrogen molecules produced. In this regard, a possible way of circumventing this issue has been also considered which involves

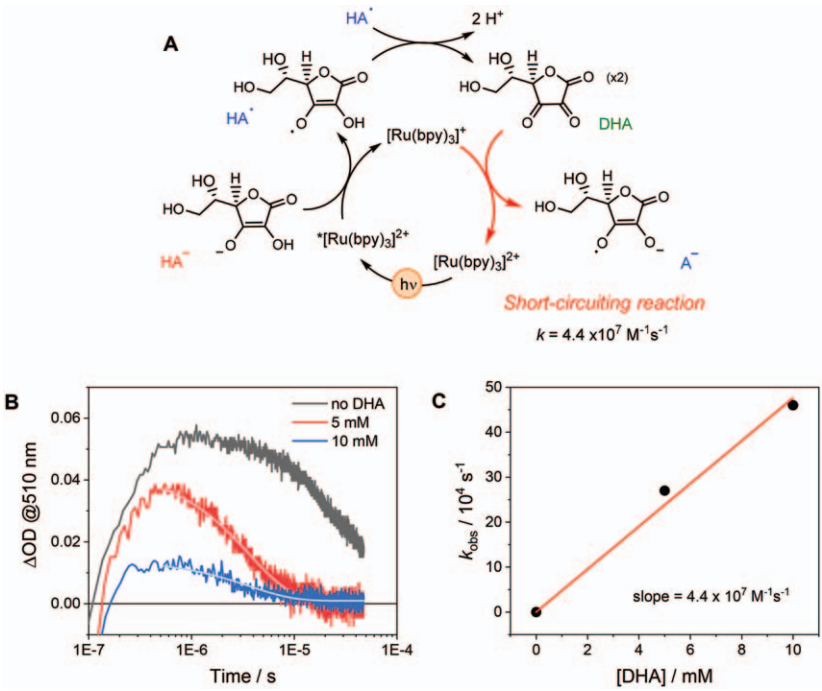

Fig. 11 (A) Schematic representation of the short-circuiting reaction involved in light-driven catalysis with ascorbate as the electron donor; (B) kinetic traces at 510 nm measured by laser flash photolysis associated with oxidation of $[Ru(bpy)_3]^{+}$ by DHA; (C) plot of the observed rate (calculated form an exponential fitting of the traces in Fig. 11B) *vs.* DHA concentration for the estimation of the bimolecular rate constant. Adapted from ref. 64 with permission from the Royal Society of Chemistry.

the use of a secondary sacrificial electron donor such as tris(2-carboxyethyl)phosphine (TCEP).[65]

4 Conclusions

The current energy issue has stimulated tremendous efforts from the scientific community to develop novel catalysts to tackle both the oxidative and reductive side of the water splitting reaction and to apply them in light-activated cycles for conversion of solar energy into molecular fuels like dihydrogen. After many synthetic efforts spent in the past few years, the comprehension of the mechanistic aspects associated with both catalytic routines has nowadays become more relevant towards the improvement of the performances. In the present tutorial, we have shown how optical spectroscopies play a leading role in this regard, allowing the operating mechanistic pathways of light-driven catalysis to be defined and key kinetic descriptors impacting the quantum efficiency of the processes to be extracted. In particular, as per the case studies described here, the investigation of the effects of many external variables, such as buffer composition and concentration, solution pH, ionic strength, *etc.* appears critical in order to gain detailed insights into the light-driven catalytic reactions, pointing out, *e.g.*, detrimental side phenomena or PCET processes relevant to multi-electronic catalysis. We believe that other research fields such as CO_2 reduction or fixation, N_2 reduction, *etc.* would benefit from the adoption of such a conscious, methodological approach since a clear understanding of reactivity will definitely improve reaction performance.

Acknowledgements

Financial support from the Italian MUR (PRIN 2020927WY3 Electro-Light4Value, to M. N.; PRIN 2022KPK8WM PROMETEO, to A. S.), by the European Union – Next Generation UE (PRIN2022 PNRR PHOTOCORE, P2022ZSPWF to both M. N. and A. S.), from the Fondazione Cariparo (Project "SYNERGY", Ricerca Scientifica di Eccellenza 2018, to A. S.) and from the University of Ferrara (FAR2023 to M. N.) is greatfully acknowledged.

References

1 D. I. A. McKay, A. Staal, J. F. Abrams, R. Winkelmann, B. Sakschewski, S. Loriani, I. Fetzer, S. E. Cornell, J. Rockström and T. M. Lenton, *Science*, 2022, **377**, eabn7950.
2 S. I. Zandalinas, F. B. Fritschi and R. Mittler, *Trends Plant Sci.*, 2021, **26**, 588.
3 H. Ishaq, I. Dincer and C. Crawford, *Int. J. Hydrogen Energy*, 2022, **47**, 26238.
4 R. Matheu, P. Garrido-Barros, M. Gil-Sepulcre, M. Z. Ertem, X. Sala, C. Gimbert-Suriñach and A. Llobet, *Nat. Rev. Chem.*, 2019, **3**, 331.
5 S. Wang, A. Lu and C. J. Zhong, *Nano Convergence*, 2021, **8**, 4.
6 J. Yano and V. Yachandra, *Chem. Rev.*, 2014, **114**, 4175.
7 P. Greife, M. Schonborn, M. Capone, R. Assuncao, D. Narzi, L. Guidoni and H. Dau, *Nature*, 2023, **617**, 623.
8 W. Lubitz, H. Ogata, O. Ru and E. Reijerse, *Chem. Rev.*, 2014, **114**, 4081.

9 W. T. Eckenhoff, *Coord. Chem. Rev.*, 2018, **373**, 295.
10 J. L. Dempsey, B. S. Brunschwig, J. R. Winkler and H. B. Gray, *Acc. Chem. Res.*, 2009, **42**, 1995.
11 Y. Pellegrin and F. Odobel, *C. R. Chim.*, 2017, **20**, 283.
12 F. Droghetti, A. Amati, A. Ruggi and M. Natali, *Chem. Commun.*, 2024, **60**, 658.
13 A. Volpe, C. Tubaro, M. Natali, A. Sartorel, G. W. Brudvig and M. Bonchio, *Inorg. Chem.*, 2019, **58**, 16537.
14 F. Lucarini, J. Fize, A. Morozan, F. Droghetti, E. Solari, R. Scopelliti, M. Marazzi, M. Natali, M. Pastore, V. Artero and A. Ruggi, *Sustainable Energy Fuels*, 2023, **7**, 3384.
15 D. A. Kurtz and J. L. Dempsey, *Inorg. Chem.*, 2019, **58**, 16510.
16 T. Gobbato, G. A. Volpato, A. Sartorel and M. Bonchio, *Chem. Sci.*, 2023, **14**, 12402.
17 V. Balzani and A. Juris, *Coord. Chem. Rev.*, 2001, **211**, 97.
18 P. Ceroni, G. Bergamini and V. Balzani, *Angew. Chem., Int. Ed.*, 2009, **48**, 8516.
19 M. Natali, F. Nastasi, F. Puntoriero and A. Sartorel, *Eur. J. Inorg. Chem.*, 2019, 2027.
20 F. Puntoriero, S. Serroni, G. La Ganga, A. Santoro, M. Galletta, F. Nastasi, E. La Mazza, A. M. Cancelliere and S. Campagna, *Eur. J. Inorg. Chem.*, 2018, 3887.
21 H. S. White, W. G. Becker and A. J. Bard, *J. Phys. Chem.*, 1984, **88**, 1840.
22 A. Sartorel, M. Carraro, G. Scorrano, R. De Zorzi, S. Geremia, N. D. McDaniel, S. Bernhard and M. Bonchio, *J. Am. Chem. Soc.*, 2008, **130**, 5006.
23 Y. V. V. Geletii, B. Botar, P. Kögerler, D. A. A. Hillesheim, D. G. G. Musaev and C. L. L. Hill, *Angew. Chem., Int. Ed.*, 2008, **47**, 3960.
24 Y. Liu, S. Guo, A. M. Bond, J. Zhang, Y. V Geletii and C. L. Hill, *Inorg. Chem.*, 2013, **52**, 11986.
25 S. Piccinin, A. Sartorel, G. Aquilanti, A. Goldoni, M. Bonchio and S. Fabris, *Proc. Natl. Acad. Sci. U. S. A.*, 2013, **110**, 4917.
26 M. Natali, M. Orlandi, S. Berardi, S. Campagna, M. Bonchio, A. Sartorel and F. Scandola, *Inorg. Chem.*, 2012, **51**, 7324.
27 M. Burian, Z. Syrgiannis, G. La Ganga, F. Puntoriero, M. Natali, F. Scandola, S. Campagna, M. Prato, M. Bonchio, H. Amenitsch and A. Sartorel, *Inorg. Chim. Acta*, 2017, **454**, 171.
28 M. Orlandi, R. Argazzi, A. Sartorel, M. Carraro, G. Scorrano, M. Bonchio and F. Scandola, *Chem. Commun.*, 2010, **46**, 3152.
29 J. Fielden, J. M. Sumliner, N. Han, Y. V. Geletii, X. Xiang, D. G. Musaev, T. Lian and C. L. Hill, *Chem. Sci.*, 2015, **6**, 5531.
30 E. Rossin, M. Bonchio, M. Natali and A. Sartorel, *Sustainable Energy Fuels*, 2024, DOI: 10.1039/D4SE00146J.
31 U. S. Akhtar, E. L. Tae, Y. S. Chun, I. C. Hwang and K. B. Yoon, *ACS Catal.*, 2016, **6**, 8361.
32 M. W. Kanan and D. G. Nocera, *Science*, 2008, **321**, 1072.
33 E. Pizzolato, M. Natali, B. Posocco, A. Montellano López, I. Bazzan, M. Di Valentin, P. Galloni, V. Conte, M. Bonchio, F. Scandola and A. Sartorel, *Chem. Commun.*, 2013, **49**, 9941.
34 S. Berardi, G. La Ganga, M. Natali, I. Bazzan, F. Puntoriero, A. Sartorel, F. Scandola, S. Campagna and M. Bonchio, *J. Am. Chem. Soc.*, 2012, **134**, 11104.
35 S. M. Lauinger, Q. Yin, Y. V. Geletii and C. L. Hill, *Adv. Inorg. Chem.*, 2017, **69**, 117.
36 G. A. Volpato, A. Bonetto, A. Marcomini, P. Mialane, M. Bonchio, M. Natali and A. Sartorel, *Sustainable Energy Fuels*, 2018, **2**, 1951.

37 M. Grzelczak, J. Zhang, J. Pfrommer, J. Hartmann, M. Driess, M. Antonietti and X. Wang, *ACS Catal.*, 2013, **3**, 383.
38 J. W. Vickers, H. Lv, J. M. Sumliner, G. Zhu, Z. Luo, D. G. Musaev, Y. V. Geletii and C. L. Hill, *J. Am. Chem. Soc.*, 2013, **135**, 14110.
39 S. J. Folkman, J. Soriano-Lopez, J. R. Galán-Mascarós and R. G. Finke, *J. Am. Chem. Soc.*, 2018, **140**, 12040.
40 Q. Yin, J. M. Tan, C. Besson, Y. V. Geletii, D. G. Musaev, A. E. Kuznetsov, Z. Luo, K. I. Hardcastle and C. L. Hill, *Science*, 2010, **328**, 342.
41 Z. Huang, Z. Luo, Y. V. Geletii, J. W. Vickers, Q. Yin, D. Wu, Y. Hou, Y. Ding, J. Song, D. G. Musaev, C. L. Hill and T. Lian, *J. Am. Chem. Soc.*, 2011, **133**, 2068.
42 M. Natali, S. Berardi, A. Sartorel, M. Bonchio, S. Campagna and F. Scandola, *Chem. Commun.*, 2012, **48**, 8808.
43 M. Natali, I. Bazzan, S. Goberna-Ferrón, R. Al-Oweini, M. Ibrahim, B. S. Bassil, H. Dau, F. Scandola, J. R. Galán-Mascarós, U. Kortz, A. Sartorel, I. Zaharieva and M. Bonchio, *Green Chem.*, 2017, **19**, 2416.
44 I. Bazzan, A. Volpe, A. Dolbecq, M. Natali, A. Sartorel, P. Mialane and M. Bonchio, *Catal. Today*, 2017, **290**, 39.
45 F. Rigodanza, N. Marino, A. Bonetto, A. Marcomini, M. Bonchio, M. Natali and A. Sartorel, *ChemPhysChem*, 2021, **22**, 1208.
46 D. Streich, Y. Astuti, M. Orlandi, L. Schwartz, R. Lomoth, L. Hammarström and S. Ott, *Chem. – Eur. J.*, 2010, **16**, 60.
47 F. Droghetti, F. Lucarini, A. Molinari, A. Ruggi and M. Natali, *Dalton Trans.*, 2022, **51**, 10658.
48 S. Losse, J. G. Vos and S. Rau, *Coord. Chem. Rev.*, 2010, **254**, 2492.
49 B. Probst, C. Kolano, P. Hamm and R. Alberto, *Inorg. Chem.*, 2009, **48**, 1836.
50 P. Du, K. Knowles and R. Eisenberg, *J. Am. Chem. Soc.*, 2008, **130**, 12576.
51 T. Lazarides, M. Delor, I. V. Sazanovich, T. M. Mc Cormick, I. Georgakaki, G. Charalambidis, J. A. Weinstein and A. G. Coutsolelos, *Chem. Commun.*, 2014, **50**, 521.
52 M. Natali, R. Argazzi, C. Chiorboli, E. Iengo and F. Scandola, *Chem. – Eur. J.*, 2013, **19**, 9261.
53 T. Lazarides, T. Mccormick, P. Du, G. Luo, B. Lindley and R. Eisenberg, *J. Am. Chem. Soc.*, 2009, **131**, 9192.
54 M. Natali, *ACS Catal.*, 2017, **7**, 1330.
55 M. Natali, E. Badetti, E. Deponti, M. Gamberoni, F. A. Scaramuzzo, A. Sartorel and C. Zonta, *Dalton Trans.*, 2016, **45**, 14764.
56 R. Tyburski, T. Liu, S. D. Glover and L. Hammarström, *J. Am. Chem. Soc.*, 2021, **143**, 560.
57 A. Lewandowska-Andralojc, T. Baine, X. Zhao, J. T. Muckerman, E. Fujita and D. E. Polyansky, *Inorg. Chem.*, 2015, **54**, 4310.
58 A. Reynal, E. Pastor, M. A. Gross, S. Selim, E. Reisner and J. R. Durrant, *Chem. Sci.*, 2015, **6**, 4855.
59 M. O. Hagan, M. Ho, J. Y. Yang, A. M. Appel, M. R. Dubois, S. Raugei, W. J. Shaw, D. L. Dubois and R. M. Bullock, *J. Am. Chem. Soc.*, 2012, **134**, 19409.
60 R. S. Khnayzer, V. S. Thoi, M. Nippe, A. E. King, J. W. Jurss, K. A. El Roz, J. R. Long, C. J. Chang and F. N. Castellano, *Energy Environ. Sci.*, 2014, **7**, 1477.
61 W. M. Singh, T. Baine, S. Kudo, S. Tian, X. A. N. Ma, H. Zhou, N. J. Deyonker, T. C. Pham, J. C. Bollinger, D. L. Baker, B. Yan, C. E. Webster and X. Zhao, *Angew. Chem., Int. Ed.*, 2012, **51**, 5941.

62 F. Lucarini, M. Pastore, S. Vasylevskyi, M. Varisco, E. Solari, A. Crochet, K. M. Fromm, F. Zobi and A. Ruggi, *Chem. – Eur. J.*, 2017, **23**, 6768.
63 F. Lucarini, J. Fize, A. Morozan, M. Marazzi, M. Natali, M. Pastore, V. Artero and A. Ruggi, *Sustainable Energy Fuels*, 2020, **4**, 589.
64 E. Deponti, A. Luisa, M. Natali, E. Iengo and F. Scandola, *Dalton Trans.*, 2014, **43**, 16345.
65 C. Bachmann, B. Probst, M. Guttentag and R. Alberto, *Chem. Commun.*, 2014, **50**, 6737.